I&EC research
Industrial & Engineering Chemistry Research

Article

Cite This: Ind. Eng. Chem. Res. 2019, 58, 836−848

pubs.acs.org/IECR

# Synthesis and Characterization of ZnNiIn Layered Double Hydroxides Derived Mixed Metal Oxides with Highly Efficient Photoelectrocatalytic Activities

Duo Pan,[†] Shengsong Ge,[*,†] Junkai Zhao,[†,‡] Jiangyang Tian,[†] Qian Shao,[†] Lin Guo,[†] Xianmin Mai,[*,§] Tingting Wu,[∥] Vignesh Murugadoss,[‡,⊥] Hu Liu,[‡,#] Tao Ding,[*,▽] Subramania Angaiah,[*,⊥] and Zhanhu Guo[*,‡]

[†]College of Chemical and Environmental Engineering, Shandong University of Science and Technology, Qingdao 266590, China

[‡]Integrated Composites Laboratory (ICL), Department of Chemical & Biomolecular Engineering, University of Tennessee, Knoxville, Tennessee 37996, United States

[§]School of Urban Planning and Architecture, Southwest Minzu University, Chengdu 610041, China

[∥]Department of Civil and Environmental Engineering, The University of Alabama, Huntsville, Alabama 35899, United States

[⊥]Electrochemical Energy Research Lab, Centre for Nanoscience and Technology, Pondicherry University, Puducherry 605 014, India

[#]Key Laboratory of Materials Processing and Mold (Zhengzhou University), Ministry of Education; National Engineering Research Center for Advanced Polymer Processing Technology, Zhengzhou University, Zhengzhou 450002, China

[▽]College of Chemistry and Chemical Engineering, Henan University, Kaifeng 475004, China

**ABSTRACT:** Visible-light-responsive ZnO/NiO/$In_2O_3$ mixed metal oxide (ZNI-MMO) photoelectrocatalysts with different Ni/In molar ratios were derived from corresponding ternary hydrotalcite-like precursors followed by calcination at 600 °C. The as-obtained samples were characterized by XRD, TGA, BET, XPS, SEM, TEM, and UV−vis spectra techniques. The optimal molar ratio of Ni/In was found to be 1:1, where the sample (ZNI-1-MMO) was formed by the aggregation of nanospheres with an average diameter of about 50 nm and a BET specific surface area of 33.80 $m^2/g$. With a 1.5 V bias potential, the ZNI-1-MMO photoelectrode exhibited high photoelectrocatalytic activity toward methylene blue (MB) degradation. The photoelectrocatalytic degradation of MB followed pseudo-first-order kinetics. Radical trapping experiments were conducted to probe the reactive species in the degradation processes. Results indicated that $h^+$ and $^{\bullet}OH$ may be responsible for the efficient MB removal. The photoelectrodegradation mechanism of MB by ZNI-1-MMO-1.5 V photoelectrode was also discussed.

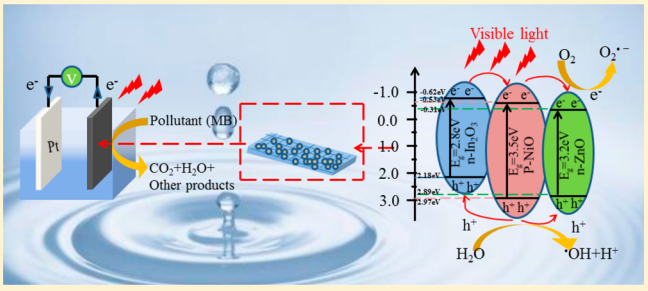


## 1. INTRODUCTION

With the rapid industrial and economic development, environmental pollution has become more and more severe in recent years. As a major contributor to industrial wastewater, dyeing wastewater has posed a threat to the ecosystem as well as human health. Therefore, it is of great importance to efficiently treat dyeing industry wastewater. Although effective removal of organic dyes from industrial wastewater has received more interest, it has always been a challenging task for environmental engineers. Conventional dye wastewater treatment methods include physical adsorption, chemical oxidation, and biological treatment.[1−3] However, many of these methods suffer limited efficiencies, operational constraints, and/or secondary pollution.[4,5]

Advanced oxidation processes (AOPs) have emerged as a new method to treat refractory pollutants.[6] AOPs usually rely on in situ generation of hydroxyl radicals, a strong and nonselective oxidant, to oxidize and even mineralize organic pollutants.[7,8] Among various AOPs, photocatalysis (PC)/electrocatalysis (EC)/photoelectrocatalysis (PEC) have the advantages of low chemical consumption, simple operation, and high efficiencies.[9−13] However, the recovery and reusability of photocatalysts is often a problem especially when the catalysts of small size are dispersed into the liquid phase for a high reactive surface area.[14] For electrochemical catalytic systems, the energy efficiency needs to be increased for the process to be cost-effective.[15] However, the synergistic photoelectric catalytic method, which combines photocatalysis and electrochemical technologies and compensates for the

Received: October 2, 2018
Revised: December 8, 2018
Accepted: December 21, 2018
Published: December 21, 2018






DOI: 10.1021/acs.iecr.8b04829
Ind. Eng. Chem. Res. 2019, 58, 836−848

deficiencies both these, has shown great advantages in degrading organic pollutants in industrial wastewater.[16,17]

PEC involves generation and separation of electron−hole pairs which occurs on the semiconductor electrode under light illumination.[18] Under a bias voltage, electrons in the semiconductor (photovoltaic anode) move toward the cathode through an external circuit while the holes move toward the semiconductor/electrolyte interface, where they can oxidize the substances present in the solution.[19,20] Since Fujishima and Honda carried out the pioneering work on the decomposition of water by $TiO_2$ photochemical electrode under UV irradiation, the photocatalytic semiconductors had been unfolded around the world.[21,22] Subsequently, some photoelectrode materials such as ZnO,[23] NiO,[24] and $Cu_2O$[25] have also been developed for photocatalytic oxidation. For example, the $Cu_2O$ micronanocrystals were prepared through liquid phase reduction method by Zhu et al. and demonstrated a degradation efficiency of RhB of 56.3% under visible light irradiation.[26] Zhao et al. used sunflower pollen as a biological template to prepare $TiO_2$ hollow microspheres doped with a small amount of ZrO, which achieved 96.0% degradation of RhB under ultraviolet light irradiation.[27] However, these catalysts not only require complicated synthesis processes (e.g., electrodeposition, template method, and multiple anodization) but also need activation by ultraviolet light due to their large band gap.[28] Therefore, it is of great importance to develop a visible light responsive photocatalyst with stable performance via a facile synthesis procedure.

Layered double hydroxides (LDHs) and synthetic hydrotalcite-like materials belong to the family of anionic clays having a natural brucite-like layered structure.[29] The generalized chemical formula of LDHs is $[M^{2+}_{(1-x)}M^{3+}_{x}(OH)_2]^{x+}[A^{n-}_{x/n}]\cdot mH_2O$, where $M^{2+}$ and $M^{3+}$ represent divalent ($Mg^{2+}$, $Zn^{2+}$, $Co^{2+}$, $Cu^{2+}$, $Ni^{2+}$, $Mn^{2+}$, etc.) and trivalent ($Al^{3+}$, $Fe^{3+}$, $Ga^{3+}$, $Cr^{3+}$, $V^{3+}$, $Ti^{3+}$, etc.) metal cations, respectively; $A^{n-}$ stands for the interlayer anions ($NO_3^-$, $Cl^-$, $OH^-$, $CO_3^{2-}$, $SO_4^{2-}$, etc.).[30−32] The LDHs have a very broad chemical composition and a special layered structure, which enables potential applications as catalysts, catalyst supports, and ion exchangers/adsorbents.[33,34] Furthermore, the LDH materials were calcined at moderate temperatures (300−600 °C) to form highly active mixed metal oxide (MMO) nanocomposites with thermal stability and high specific surface area.[35] The obtained composite binary or ternary MMOs showed a smaller band gap than the single semiconductor oxides in the composition, which can promote photoelectron transfer to the photocatalyst surface under visible light conditions.[36] For example, Zhang et al. have recently investigated the effects of different Zn/Ni/Al molar ratios on the photocatalytic properties of ZnNiAl-MMO and demonstrated a maximum of 97.3% photocatalytic decoloration efficiency at Zn/Ni/Al molar ratio of 2:1:1.[37] Huang et al. synthesized ternary CoMnFe-MMO with a coprecipitation method and exhibited a better MB degrading capability of 92.0% under visible light illumination for 60 min much higher than that of the binary CoFe-MMO.[38] Although they have been widely studied as photocatalysts, MMO materials are rarely used as photoelectrocatalytic materials to degrade organic contaminants.

In this work, a series of ZnNiIn MMOs (ZNI-MMOs) were synthesized by a simple hydrothermal method at different molar ratios of Ni/In, which were then comprehensively characterized using a suite of characterization techniques. The photoelectrocatalytic performance of the ZNI-MMOs was tested in MB degradation experiments with a bias potential under visible light irradiation. Results indicate that ZNI-1-MMO (Ni/In = 1:1) photoelectrode can not only efficiently degrade organic pollutant MB but also conveniently be reused. This study provides new methods and insights in the development of photoelectrocatalytic materials for the degradation of organic pollutants.

## 2. EXPERIMENTAL PROCEDURES

**2.1. Materials.** Zinc nitrate [$Zn(NO_3)_2\cdot 6H_2O$], nickel nitrate [$Ni(NO_3)_2\cdot 6H_2O$], and indium nitrate [$In(NO_3)_3\cdot 4.5H_2O$] were obtained from Sinopharm Chemical Reagent Co., Ltd. (AR, Shanghai, China). Urea ($NH_2CONH_2$). Methylene blue (MB) were purchased from Tianjin Bodi Chemical Reagent Co., Ltd. (AR, Tianjin, China). Isopropyl alcohol (IPA), *p*-benzoquinone, and EDTA-2Na were provided by Chengdu Kelong Co., Ltd. (AR, Chengdu, China). Distilled water was used throughout the experiments. All reagents were analytical-grade and used without further purification.

**2.2. Catalyst Preparation.** *2.2.1. Preparation of ZNI-LDH Precursors.* ZNI-LDHs were prepared by a hydrothermal method and the molar ratio of ($Zn^{2+}$, $Ni^{2+}$)/$In^{3+}$ was specifically denoted herein as $M^{2+}/M^{3+}$. Previous studies[39,40] have demonstrated that best molar ratio of $M^{2+}/M^{3+}$ is 3:1. A detailed synthetic procedure is as follows. The indium nitrate (0.5 g) and urea (3.5 g) together with $Zn(NO_3)_2\cdot 6H_2O$, $Ni(NO_3)_2\cdot 6H_2O$ at different Ni/In molar ratios were dissolved in 80 mL of deionized water to form mixture solution under vigorous stirring. The solution was transferred into Teflon-lined autoclaves and heat-treated at 150 °C for 12 h, then the supernatant was poured off and the precipitate was washed with distilled water until pH 7. Finally, the as-obtained precipitate was dried in an oven at 60 °C overnight to obtain ZNI-LDH precursors. Precursors with Ni/In molar ratios of 0:1 and 3:1 are ZnIn-LDH and NiIn-LDH, respectively, and are correspondingly denoted as ZI-LDH and NI-LDH. Precursors with Ni/In molar ratios of 1:1 and 2:1 are denoted as ZNI-1-LDH and ZNI-2-LDH. Hence, ZI-LDH and NI-LDH belong to binary hydrotalcites, while ZNI-1-LDH and ZNI-2-LDH belong to ternary hydrotalcites.

*2.2.2. Preparation of ZNI-MMOs.* ZNI-LDH precursors were calcined in a muffle furnace at 600 °C in air for 4 h at a ramping rate of 5 °C/min. After the muffle furnace naturally cooled down to room temperature, the ZNI-MMOs were obtained. The calcined samples with Ni/In molar ratios of 0:1 and 3:1 are ZnIn-MMO and NiIn-MMO, respectively, which are correspondingly denoted as ZI-MMO and NI-MMO. The calcined samples with Ni/In molar ratios of 1:1 and 2:1 are denoted as ZNI-1-MMO and ZNI-2-MMO respectively. In addition, pure ZnO, NiO, and InO metal oxide particles were synthesized in the same manner.

**2.3. Characterization.** The crystal structures of the samples were determined by X-ray diffraction (XRD, ultima IV, Rigaku, Japan), and 2$\theta$ ranged from 10 to 70°, with Cu K$\alpha$ radiation ($\lambda$ = 0.1540 nm). Elemental composition analysis of the samples was performed on an ESCALAB 250Xi X-ray photoelectron spectrometer (XPS, Thermo Scientific, USA) with Al K$\alpha$ radiation (150 W, 15 kV, and 1486 eV). The thermogravimetric analyses were performed on a thermal analyzer (TGA 851e Mettler). The morphological features of the samples were investigated by scanning electron microscopy


DOI: 10.1021/acs.iecr.8b04829
Ind. Eng. Chem. Res. 2019, 58, 836−848

(SEM, S-4800, Hitachi, Japan) and transmission electron microscope (TEM, JEM-2100F, Japan). The specific surface area and pore volume and size were calculated by the Brunauer–Emmett–Teller (BET, Tristar II 3020, Micromeritics, America) method.The band gap of the products was determined from UV–Vis absorption spectra on a UV–vis spectrophotometer (UV–Vis DRS, UV9000, METASH, China).

**2.4. Photocatalytic Activity Performance Tests.** The photocatalytic activity of ZNI-MMOs with different Ni/In molar ratios was examined by MB degradation experiments. The initial concentration of MB was 20 mg/L. A 200 W xenon lamp with $\lambda$ = 320–1100 nm was used as the light source. In order to exclude the effects of UV light, a UV-blocking glass was employed. For each run, 20 mg of catalyst power was added into 100 mL of MB solution and stirred for 1 h in the dark to obtain an adsorption/desorption equilibrium. During light irradiation, the catalysts were maintained in a suspension state by a mechanical agitator. Then, 2 mL of reaction solution was extracted with a pipet every 30 min and immediately centrifuged to separate the catalysts with the solution. The concentration of MB in the solution was then measured by using a UV–vis spectrophotometer (UV9000) at a wavelength of 664 nm.

**2.5. Photoelectrocatalytic Activity Performance Tests and Photoelectrochemical Measurements.** For photoelectrocatalytic experiments, a nickel foam (4 $cm^2$) coated with 20 mg of catalyst was used as the anode and a Pt plate served as the cathode. The anode and cathode are attached to the lid of a customized cube quartz vessel. The light source was placed 15 cm away from the anode and different bias voltages were supplied by the electrochemical workstation (Autolab, Metrohm Co., Ltd.). The anode was connected to the working electrode of the three-electrode system, and the cathode was connected to the counter electrode and the reference electrode. A 0.1 mol/L $Na_2SO_4$ solution was used as the supporting electrolyte, and the MB concentration was 20 mg/L. The samples were taken and analyzed as described above. The photoelectrochemical (PECH) properties of the samples, such as photocurrent response and electrochemical impedance spectroscopy (EIS), were measured using the same operating system. The only difference was that an additional saturated calomel electrode was connected to the reference electrode of the three-electrode system.

## 3. RESULTS AND DISCUSSION

**3.1. Characterization of the Products.** The XRD patterns of the as-prepared ZNI-LDH precursors with different Ni/In molar ratios were shown in Figure 1. The diffraction peaks at 2$\theta$ = 11.7, 23.4, 33.4, 39.2, 46.5, 52.9, 56.3, and 60.2° correspond to (003), (006), (009), (015), (018), (1010), (0111), and (110) crystal planes of LDH, respectively.[41] All the characteristic peaks correspond to the unique layered structure of hydrotalcite.[29] The structural parameters of the ZNI-LDH precursors are listed in Table 1. The crystallite size of the samples was estimated by the Scherrer equation:[42]

$$D = k\lambda/(\beta \cos\theta) \quad (1)$$

where $D$ is the crystallite size, $k$ is the Scherrer constant ($k$ = 0.89), $\lambda$ is the X-ray wavelength, $\beta$ is the line width at half-maximum height, and $\theta$ is the half angle position of the diffraction reflex on the 2$\theta$ scale. The average crystallite sizes $D_{003}$ of ternary ZNI-1-LDH (Ni/In = 1) and ZNI-2-LDH (Ni/In = 2) were calculated to be ~17.8 and ~17.6 nm, respectively, which were slightly higher than those of binary ZI-LDH (Ni/In = 0, ~17.2 nm) and NI-LDH (Ni/In = 3, ~16.8 nm). This may be because three different type of metal particles in ternary LDHs improved the rate of grain binding and crystal growth. The other diffraction peaks of binary NI-LDH shifted slightly to the right compared to those of the other three samples. It is mainly attributed to the fact that NI-LDH has a smaller crystallite size at other diffraction peaks. According to the Bragg equation,[43] 2$D$ sin $\theta$ = $n\lambda$, as the crystallite size ($D$) becomes smaller, the diffraction angle ($\theta$) increases correspondingly. This is well-illustrated by the (006) peak shown in Figure 1 and the crystallite size of $D_{006}$ in Table 1. All samples belong to the hexagonal system, and the lattice parameters $a$ and $c$ of LDHs were calculated using the correlation formulas $a = 2D_{110}$ and $c = 3D_{003}$.[44]

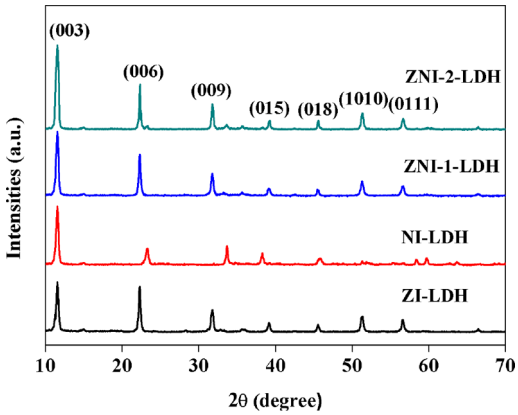


**Figure 1.** XRD patterns of the as-synthesized ZNI-LDHs with different Ni/In mole ratios.

**Table 1. Structural Parameters of ZNI-LDH Precursors**

| precursors | $Zn^{2+}/Ni^{2+}/In^{3+}$ nominal ratio | $D_{003}$ (nm)[a] | $D_{006}$ (nm)[a] | lattice parameters (nm)[b] | |
|---|---|---|---|---|---|
| | | | | $a$ | $c$ |
| ZI-LDH | 3:0:1 | 17.2 | 11.1 | 0.3174 | 2.3102 |
| NI-LDH | 0:3:1 | 16.8 | 8.50 | 0.3176 | 2.3165 |
| ZNI-1-LDH | 2:1:1 | 17.8 | 14.3 | 0.3177 | 2.2892 |
| ZNI-2-LDH | 1:2:1 | 17.6 | 13.4 | 0.3153 | 2.3058 |

[a]The crystallite size ($D$) calculated from (003) and (006) reflection using the Scherrer equation. [b]$a$ = 2D110, $c$ = 3D003.

Figure 2 shows the XRD patterns of the ZNI-MMOs obtained after the ZNI-LDH precursors was calcined at 600 °C. As shown in Figure 2A, the diffraction characteristic peaks after calcination can be indexed to hexagonal wurtzite-structured ZnO (Powder Diffraction File (PDF) no. 36–1451, Joint Committee on Powder Diffraction Standards (JCPDS), [2015]), cubic NiO (PDF no. 44–1159, JCPDS, [2015]), and cubic $In_2O_3$ (PDF no. 06–0416, JCPDS, [2015]), respectively, which are better displayed in Figure 2B. The diffraction reflections around 2$\theta$ = 31.8, 34.4, 36.3, and 56.6° corresponds to the crystal plane of ZnO.[45] The reflections at about 37.2, 43.3, and 62.9° corresponds to the crystal plane of NiO. Four diffraction peaks at 2$\theta$ = 30.7, 35.5, 51.1, and 60.8° in all samples are indexed to the cubic phase of $In_2O_3$.[46]

Figure 3 shows the thermal analysis of ZNI-LDHs before calcination. Generally, there are four stages of mass loss,


DOI: 10.1021/acs.iecr.8b04829
Ind. Eng. Chem. Res. 2019, 58, 836–848

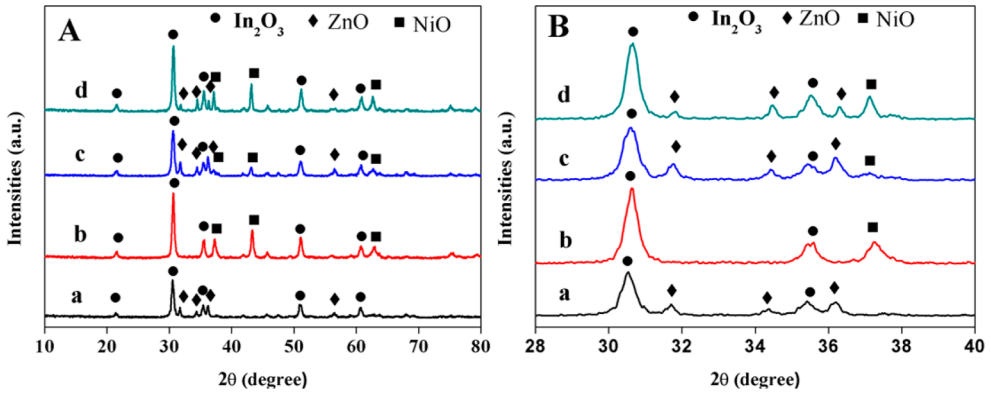


**Figure 2.** (A) XRD patterns of (a) ZI-MMO, (b) NI-MMO, (c) ZNI-1-MMO, and (d) ZNI-2-MMO; (B) the densely diffracted sections from 28 to 40° enlarged and refined of the samples.

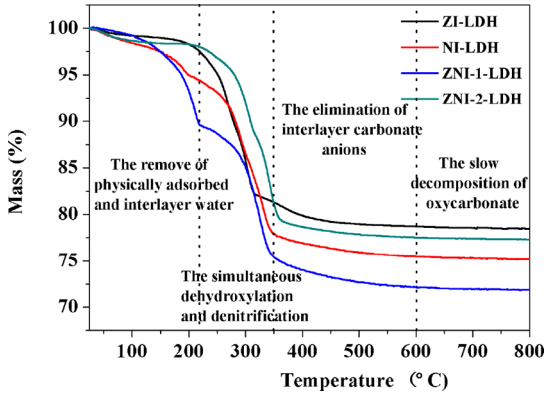


**Figure 3.** TGA curves of the as-synthesized ZNI-LDHs with different Ni/In mole ratios.

located in the temperature ranges of 25−220 °C, 220−350 °C, 350−600 °C, and 600−800 °C. The first stage of mass loss corresponds to the volatilization of water molecules coming from the external surfaces and internal crystallites of the LDH precursors.[47] The second is due to simultaneous dehydroxylation of OH groups and denitrification of urea resulting in a mass loss of 15.43%.[48] The third mass loss is due to the slow decomposition of the carbonate in the ZNI-LDHs to release oxygen and $CO_2$.[49] At temperatures above 600 °C, mixed metal oxides started to form and the sample mass is essentially unchanged because of the slow decomposition of oxycarbonate.[50]

The specific surface area and pore structure of the as-prepared samples were determined by BET measurements (Figure 4). The shape of the adsorption−desorption isotherm appears to be close to type IV isotherm according to the IUPAC classification.[51] The specific surface areas and pore structure data of all samples are shown in Table 2. Compared

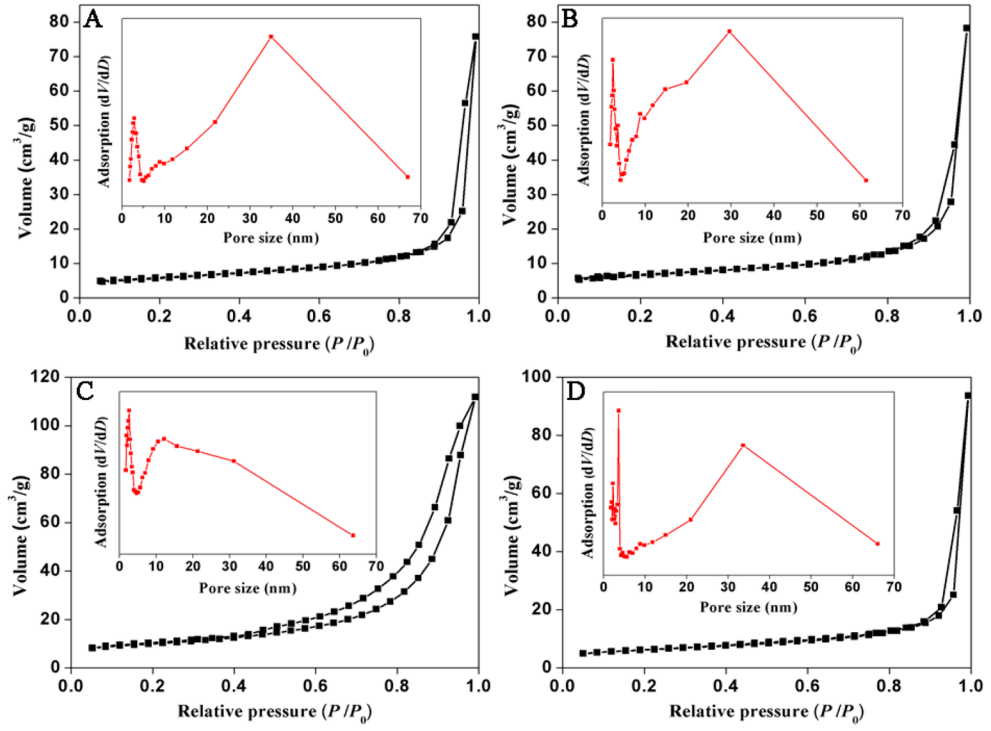


**Figure 4.** $N_2$ sorption isotherms and pore size distribution of (A) ZI-MMO, (B) NI-MMO, (C) ZNI-1-MMO, and (D) ZNI-2-MMO.



DOI: 10.1021/acs.iecr.8b04829
Ind. Eng. Chem. Res. 2019, 58, 836−848

**Table 2. Specific Surface Area and Pore Performance Data of ZNI-MMOs with Different Ni/In Mole Ratios**

| samples | surface area $S_{BET}$ ($m^2/g$)[a] | pore size (nm)[b] | pore volume ($cm^3/g$)[c] |
|---|---|---|---|
| ZI-MMO | 19.70 | 29.26 | 0.03 |
| NI-MMO | 22.56 | 27.51 | 0.04 |
| ZNI-1-MMO | 33.80 | 13.34 | 0.13 |
| ZNI-2-MMO | 21.05 | 31.77 | 0.03 |

[a]The specific surface areas ($S_{BET}$) were calculated using nitrogen adsorption data according to the BET method. [b]Pore size was estimated by applying the BJH method to the desorption branch of the isotherms. [c]Total pore volume ($V_p$) was estimated from the adsorption data at $p/p_0 = 0.95$.

to the other three samples, ZNI-1-MMO exhibits a relatively larger specific surface area (33.80 $m^2/g$) and pore volume (0.13 $cm^3/g$) but a smaller pore size (13.34 nm), which may be attributed to the crystal structure and heterojunction formation.[52]

The morphologies of the as-prepared ZNI-MMOs were investigated by SEM (Figure 5). It can be seen that the ZI-MMO is made up of agglomerated irregular round cakes with length of about 200 nm (Figure 5A). At a molar ratio of Ni/In = 3:1, the binary NI-MMO shows a brilliant ice crystal flocculent structure (Figure 5B). From Figure 5C,D, it can be seen that the morphologies of the ternary ZNI-1-MMO and ZNI-2-MMO are quite different from those of the binary ZI-MMO and NI-MMO, where nanospheres with an average diameter of about 50 nm appear. The change of morphology may be a strong evidence that the compounding of various metal oxides can change the crystal structure of a single oxide and make the whole structure regular and stable.[53]

In addition to the superior physical properties revealed by BET and SEM results, ZNI-1-MMO also exhibited the highest catalytic activity among the samples (to be discussed in later sections). Therefore, further material characterizations were focused on ZNI-1-MMO. The elemental mapping image (Figure 6B–E) and EDS spectra (Figure 6F) show the O, Zn, Ni, and In elements which were distributed homogeneously in ZNI-1-MMO, indicating that the three oxides of ZnO, NiO, and $In_2O_3$ were uniformly distributed in the sample ZNI-1-MMO.

In order to further investigate the detailed structural information, TEM analyses were carried out on ZNI-1-MMO. Figure 7A,B clearly demonstrates that the samples are formed by the aggregation of nanospheres with a measured diameter of about 50 nm, which is consistent with the observations by SEM. The high-resolution transmission electron microscopy (HRTEM) image of ZNI-1-MMO is shown in Figure 7C. The observed obvious lattice planes indicate the high crystallinity of ZNI-1-MMO. The interplanar distances of 0.261, 0.292, and 0.238 nm correspond well with the lattice spacing of wurtzite ZnO (002),[44] cubic NiO (200),[40] and cubic $In_2O_3$ (222)[54] planes, respectively. The selected area electron diffraction (SAED) pattern (Figure 7D) suggests that the mixed-metal oxides are polycrystalline, which is also supported by low peak intensities obtained in the XRD diffractograms.[55]

To analyze the chemical composition and element valence of ZNI-1-MMO, XPS analysis was performed. The full scan spectrum (Figure 8A) shows that Zn, Ni, In, and O are the main elements in ZNI-1-MMO. The C 1s peak at 284.8 eV from XPS instrument calibration element is used as the reference for calibration. The O 1s peak at 530.5 eV can be ascribed to $O^{2-}$.[56] The two strong peaks at 1022.3 and 1045.1 eV are assigned to Zn $2p_{3/2}$ and Zn $2p_{1/2}$, respectively, which are the features of $Zn^{2+}$ in ZnO (Figure 8B).[57] Two peaks around 854.8 and 872.7 eV are assigned to Ni $2p_{3/2}$ and Ni $2p_{1/2}$, respectively (Figure 8C), which indicate the existence of $Ni^{2+}$ in the ZNI-1-MMO.[58] The XPS spectrum of In 3d shows two individual peaks positioned at 444.0 and 451.6 eV (Figure

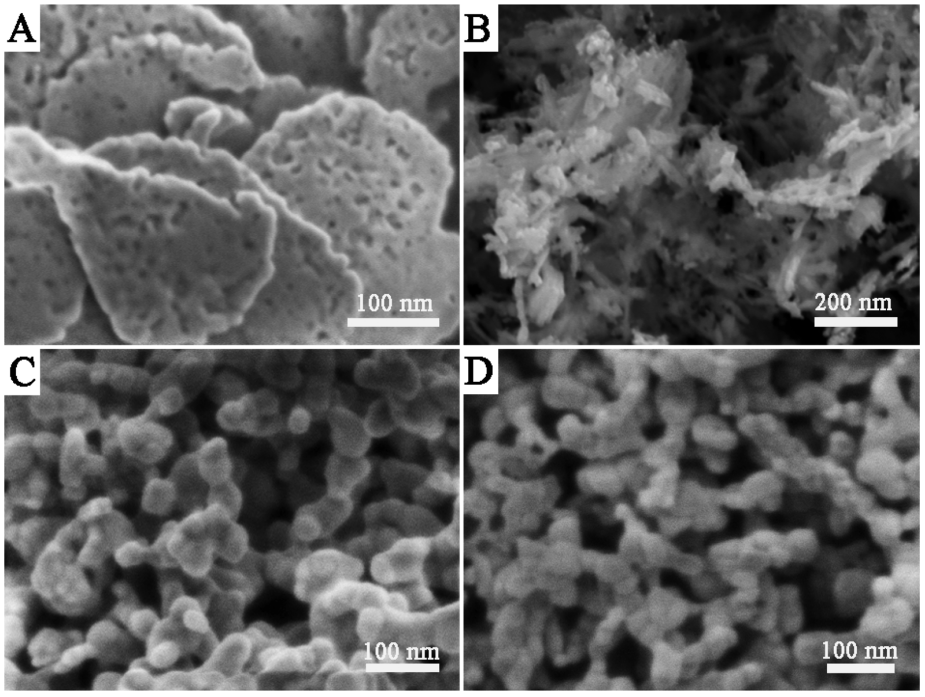


**Figure 5.** SEM images of (A) ZI-MMO, (B) NI-MMO, (C) ZNI-1-MMO, and (D) ZNI-2-MMO.



DOI: 10.1021/acs.iecr.8b04829
Ind. Eng. Chem. Res. 2019, 58, 836–848

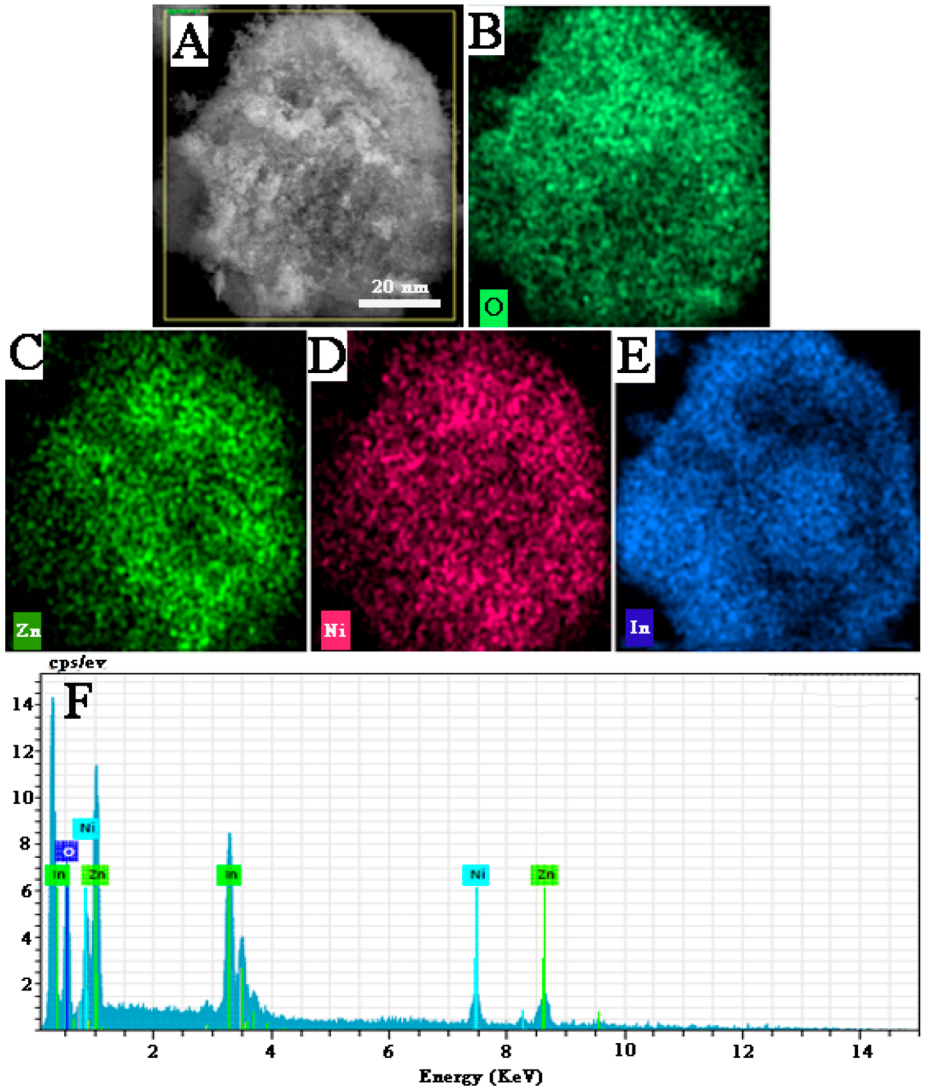


**Figure 6.** SEM images (A) of ZNI-1-MMO, elemental mapping (B–E) of ZNI-1-MMO with the homogeneous distribution of O, Zn, Ni, and In, and EDS measurement (F) of the plotted area of ZNI-1-MMO.

8D), which indicate the presence of $In^{3+}$ and can be assigned to In $3d_{5/2}$ and In $3d_{3/2}$, respectively.[54]

The UV–vis diffuse reflectance spectra of ZNI-MMO samples are shown in Figure 9A. The spectral intensity of ZNI-1-MMO, ZNI-2-MMO, and NI-MMO are observed to be higher than that of ZI-MMO because of the incorporation of $Ni^{2+}$ cation. The ZNI-MMOs also exhibit stable absorbance extended up to the full visible-light spectrum.[59] The band gap ($E_g$) of the as-prepared samples can be determined from eq 2:[27]

$$(Ah\nu)^2 = K(h\nu - E_g) \quad (2)$$

where $A$ is the absorption constant, $h\nu$ is the photon energy, $E_g$ is the band gap energy, and $K$ is a constant value. By the plot of $(Ah\nu)^2$ versus $h\nu$, the band gap ($E_g$) from the extrapolation point can be obtained.[60] In Figure 9B, the band gap value of ternary ZNI-1-MMO and ZNI-2-MMO is 2.68 and 2.91 eV, respectively, which are lower than binary ZI-MMO (3.15 eV) and NI-MMO (3.06 eV). This may be due to the mutual coupling between the different phases of ZnO, NiO, and $In_2O_3$ and formation of special heterojunction structures.[61]

**3.2. Photocatalytic Activity.** The photocatalytic activities of the samples under different experimental conditions are shown in Figure 10. After stirring for 1 h in the dark, the adsorption–desorption of MB onto the photocatalysts reached equilibrium and less than 20% MB was adsorbed for all samples tested. In order to eliminate the interference of adsorption, the dye concentration after adsorption for 1 h was taken as the new initial concentration for photocatalysis. After illumination for 3 h, photolysis (only visible light irradiation, no solid catalysts) achieved 23.0% MB degradation while adsorption by ZN1-MMO (only solid catalysts, in dark) removed 18.9% of MB. Ternary ZNI-MMOs generally exhibited photocatalytic performance better than those of the binary ZI-MMO (73.3%) and NI-MMO (56.8%) as well as pure metal oxide particles, i.e., ZnO particles (55.4%), NiO particles (50.9%), and $In_2O_3$ particles (63.9%). It is well-known that the interfacial heterojunctions could facilitate the transfer of photogenerated carriers and accelerate the degradation of dyes.[62] In addition, the degradation efficiency of ternary ZNI-1-MMO (88.5%) is higher than that of ZNI-2-MMO (83.5%), which could be ascribed to the larger specific



DOI: 10.1021/acs.iecr.8b04829
Ind. Eng. Chem. Res. 2019, 58, 836–848

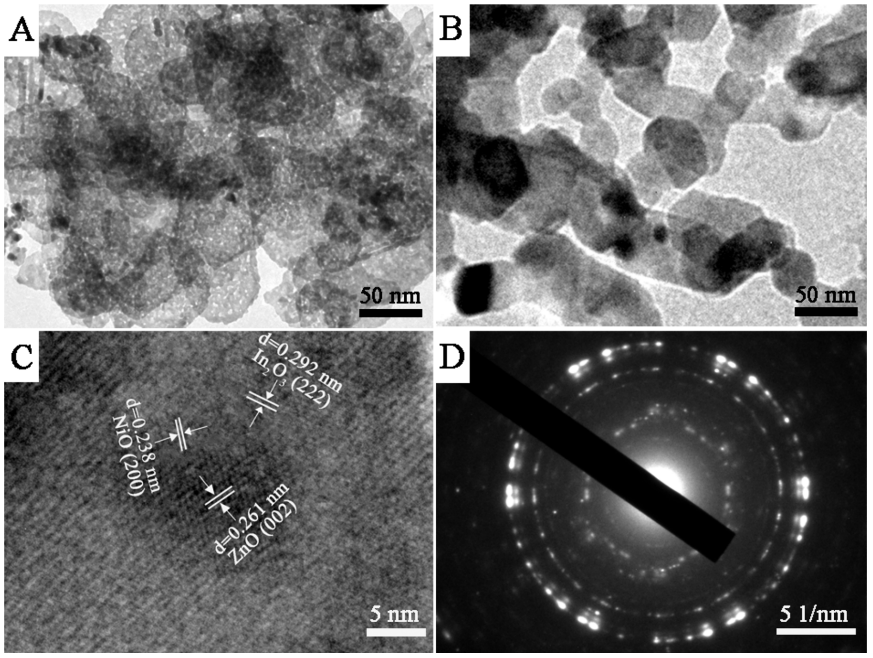


**Figure 7.** TEM images (A and B), HRTEM image (C), and SAED pattern (D) of ZNI-1-MMO.

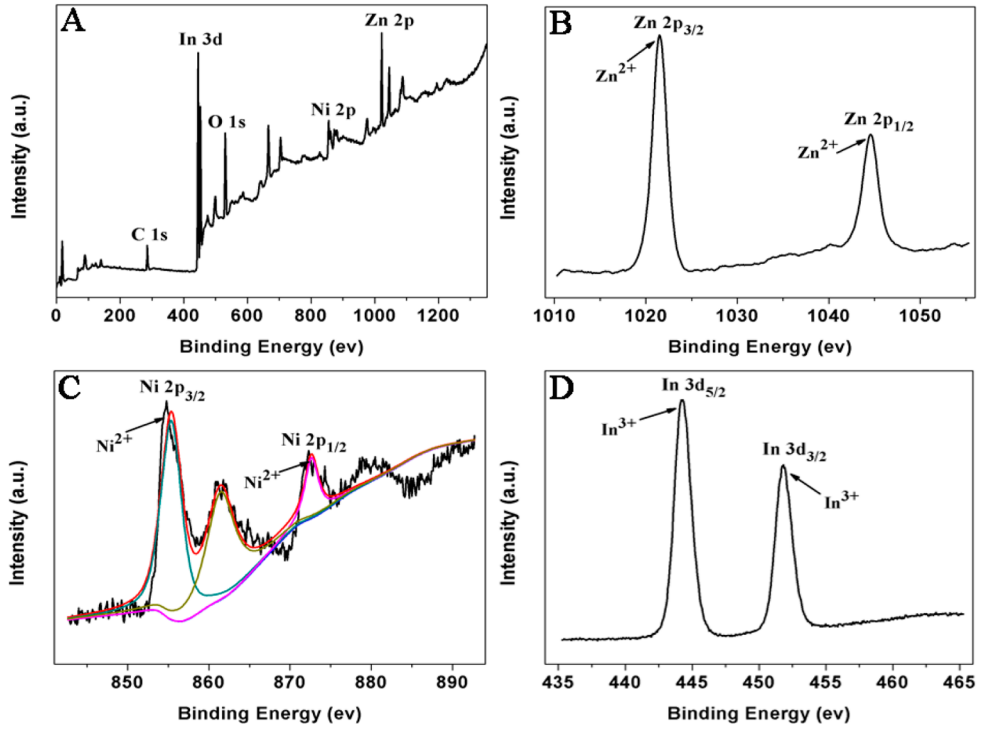


**Figure 8.** XPS full survey spectra of ZNI-1-MMO (A), the XPS spectra of Zn 2p (B), Ni 2p (C), and In 3d (D) in ZNI-1-MMO.

surface area of ZNI-1-MMO (33.80 $m^2/g$) than that of ZNI-2-MMO (21.05 $m^2/g$).

**3.3. Photoelectrocatalytic Activity.** In order to highlight the advantages of photoelectric catalysis, photocatalytic degradation, electrochemical degradation, and photoelectrocatalytic degradation of MB over ZNI-1-MMO photoelectrodes were conducted in batch reactors. As shown in Figure 11A, the ZNI-1-MMO electrode can hardly decompose MB only with a bias voltage of 0.5 V, in contrast to 81.7% of MB degradation after 3 h illumination. Furthermore, 90.9% degradation efficiency was achieved when photocatalysis and electrolysis were combined. These results indicate a bias potential of 0.5 V may only drive very limited MB degradation. However, when both light illumination and a forward bias voltage were applied to the working electrode, the photogenerated electrons can move toward the counter electrode, thus effectively reducing the recombination probability of photogenerated electrons and holes and eventually increasing the degradation efficiency.[63] It can also be seen from Figure 11B that the ZNI-1-MMO photoelectrode outperformed other ZNI-MMOs. The photo-



DOI: 10.1021/acs.iecr.8b04829
Ind. Eng. Chem. Res. 2019, 58, 836−848

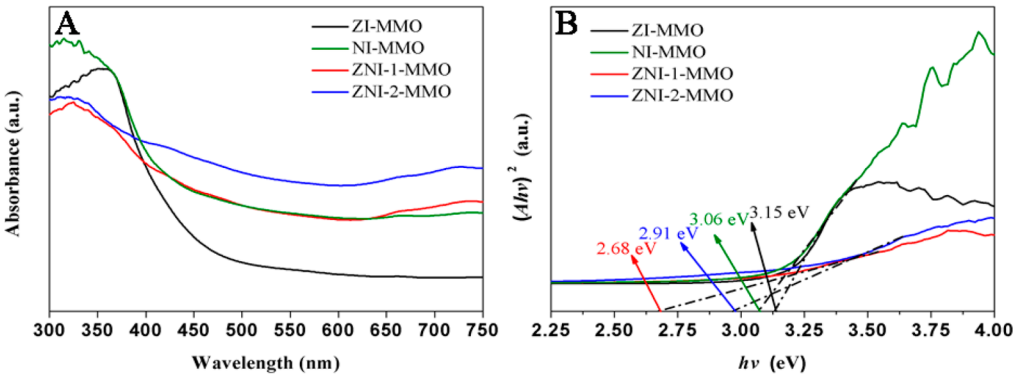


**Figure 9.** UV−vis absorption spectra (A) of the ZNI-MMOs with different Ni/In molar ratios, and the plotting of $(Ah\nu)^2$ vs $h\nu$ based on the direct transition (B).

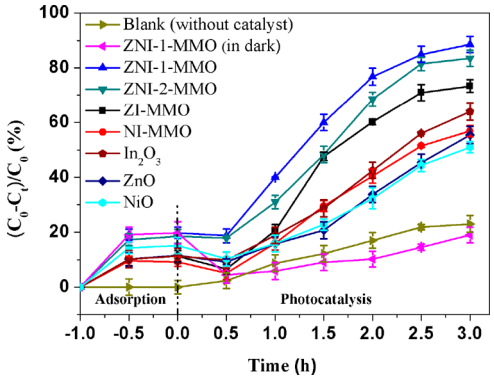


**Figure 10.** Comparison of MB degradation over NiO, ZnO, $In_2O_3$, ZNI-MMOs with different Ni/In molar ratios, and only light irradiation (without catalyst) or only catalyst (in dark).

electrocatalytic degradation kinetics of MB by ZNI-1-MMO under different bias potentials (0.5, 1.0, 1.5, and 2 V) is shown in Figure 11C. The photoelectrocatalytic degradation process follows a pseudo-first-order kinetics equation:[64]

$$\ln(C_0/C) = kt \quad (3)$$

where $C_0$ is the initial concentration of MB, $C$ is the concentration of MB at time $t$, and $k$ is the apparent first-order rate constant.

The apparent first-order rate constants ($k$) and the correlation coefficients ($R^2$) of different runs are summarized in Table 3. When the bias voltage increased from 0.5 to 1.5 V, the removal efficiency of MB increased from 90.9 to 97.2%. However, when the bias voltage further increased to 2 V, the degradation efficiency slightly decreased to 96.3%. Hence the optimum applied bias voltage for photoelectrocatalysis was 1.5 V, which could effectively promote the transfer of photogenerated electrons to the counter electrode through an external circuit and inhibit the recombination of photogenerated charges.[65] When the bias potential was too high, the number of photogenerated carriers was reduced because of the redistribution of the space charge layer, resulting in a lower degradation efficiency of MB.[14] The time-dependent UV−vis absorption spectra of MB with ZNI-1-MMO-1.5 V electrode is also shown in Figure 11D. As shown in the digital photo inset in Figure 11D, the MB aqueous solution achieved a good fading effect after 3 h of treatment.

The reusability of ZNI-1-MMO was tested in six consecutive runs for the degradation of MB with light illumination and 1.5 V bias potential. The anode and the cathode were washed with deionized water before each cycle. The results of recycling experiments were shown in Figure 12. More than 90.0% MB degradation can still be achieved after four cycles, and more than 75.0% efficiency was maintained after six cycles. The performance decrease may be related to surface deactivation caused by the adsorption of MB degradation products onto the catalysts.[40] Nonetheless, these results indicate the good reusability of the photoelectrode catalyst synthesized in this study.

**3.4. Photoelectrochemical Performance Evaluation.** As discussed above, the enhanced photoelectrocatalytic activity of the catalysts toward MB degradation may be due to the rapid interfacial transfer of photogenerated charge carries and subsequent effective charge separation. The photoelectrochemical behaviors of ZNI-MMOs before and after applied bias voltage (1.5 V) were investigated by measuring the photocurrent response in 0.1 M $Na_2SO_4$ electrolyte under intermittent visible light irradiation. As shown in the transient photocurrent ($I$−$t$) curves of Figure 13A, the ZNI-1-MMO photoelectrode demonstrated a stronger transient photocurrent response under visible light illumination, which was consistent with its better photocatalytic performance. Upon a 1.5 V bias voltage applied, improved photocurrent responses can be clearly observed (Figure 13B). The photocurrent density of ZNI-1-MMO-1.5 V photoelectrode was 0.54 mA/cm$^2$, which was higher than those of ZNI-2-MMO-1.5 V (0.52 mA/cm$^2$), ZNI-0-MMO-1.5 V (0.41 mA/cm$^2$), and ZNI-3-MMO-1.5 V (0.36 mA/cm$^2$). Meanwhile, $I$−$V$ curves were measured under the same conditions (Figure 13C), which further confirmed the higher photocurrent response of the ZNI-1-MMO-1.5 V. Electrochemical impedances spectroscopy (EIS) measurements were conducted to evaluate the charge transfer property. As shown in Figure 13D, all Nyquist diagrams have the normal arc shape, representing the significant impedance spectra of the heterojunction capacitance and resistance parallel circuit.[66,67] Among the four samples, the EIS Nyquist plot of the ZNI-1-MMO-1.5 V electrode shows the smallest arc radius, indicating its minimal resistance for interfacial charge transfer.[14] The highest photocurrent density and the minimal interfacial charge transfer resistance of ZNI-1-MMO-1.5 V photoelectrodes signified an improved photoelectrocatalytic efficiency of organic pollutant degradation.

**3.5. Photoelectrodegradation Mechanism.** The active radicals (e.g., $^{\bullet}OH$, $O_2^{\bullet-}$, $h^+$) produced by the photoelectrode


DOI: 10.1021/acs.iecr.8b04829
Ind. Eng. Chem. Res. 2019, 58, 836−848

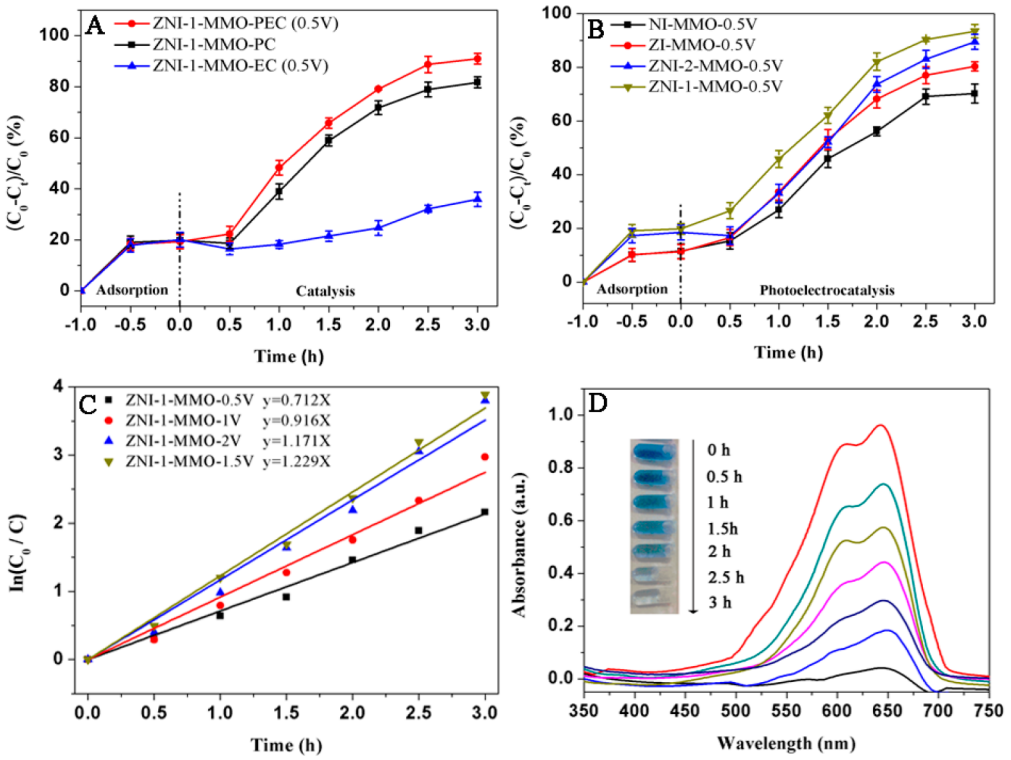


**Figure 11.** PC, EC (0.5 V), and the PEC (0.5 V) degradations of MB over the ZNI-1-MMO electrode (A), the PEC (0.5 V) degradations of MB over the ZNI-MMO electrodes with different Ni/In molar ratios (B), the photoelectrodegradation kinetic curves of ZNI-1-MMO electrode with different Ni/In molar ratios at different bias voltages (C), and the time-dependent UV−vis absorption spectra of MB with the use of ZNI-1-MMO-1.5 V (D).

**Table 3. Kinetic Constant *k* of MB Photoelectrocatalytic Degradation under Different Bias Voltages by Using ZNI-1-MMO Catalysts**

| bias voltages | $K$ ($h^{-1}$) | $R^2$ | efficiency (%)[a] |
|---|---|---|---|
| 0.5 | 0.712 | 0.9929 | 90.9 |
| 1 | 0.916 | 0.9890 | 93.5 |
| 1.5 | 1.229 | 0.9928 | 97.2 |
| 2 | 1.171 | 0.9871 | 96.3 |

[a]The degradation efficiency of MB dye by using ZNI-1-MMO catalysts under visible light irradiation for 3 h.

during the degradation process are the key reactive species for the degradation of organic pollutants.[68] In order to determine which radical plays a dominant role in the photoelectrocatalytic degradation of MB by ZNI-1-MMO-1.5 V, 1 mM isopropyl alcohol (IPA), *p*-benzoquinone, and EDTA-2Na were used as the scavenger for hydroxyl radicals, superoxide radicals, and holes respectively. Figure 14 shows the trapping experiment results. It can be seen from the histogram that all the scavenging agents added affected the degradation of MB to a certain extent. With the addition of *p*-benzoquinone, the degradation efficiency of MB decreased from 97.2 to 82.4%, while after adding IPA and EDTA-2Na, the degradation efficiency was only 31.3 and 42.4% after 3 h treatment, respectively. It can be inferred that $^{\bullet}OH$ and $h^+$ play a major role in the degradation of MB.

The proposed mechanism of photoelectrodegradation of MB by ZNI-1-MMO-1.5 V photoelectrodes was shown in

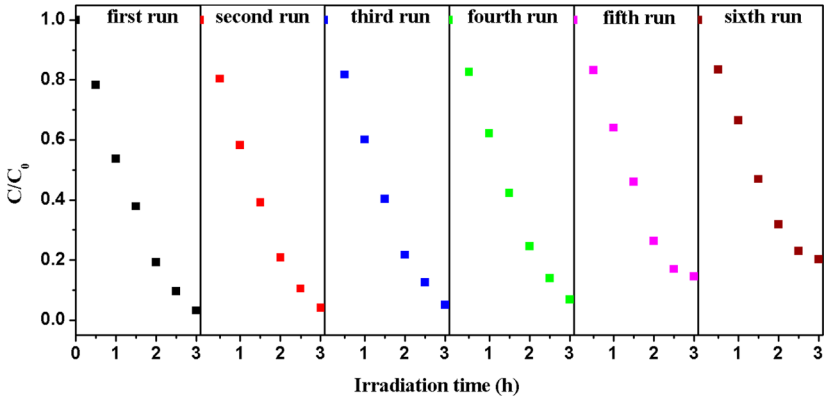


**Figure 12.** Recycling use of ZNI-1-MMO-1.5 V for dye degradation.



DOI: 10.1021/acs.iecr.8b04829
*Ind. Eng. Chem. Res.* 2019, 58, 836−848

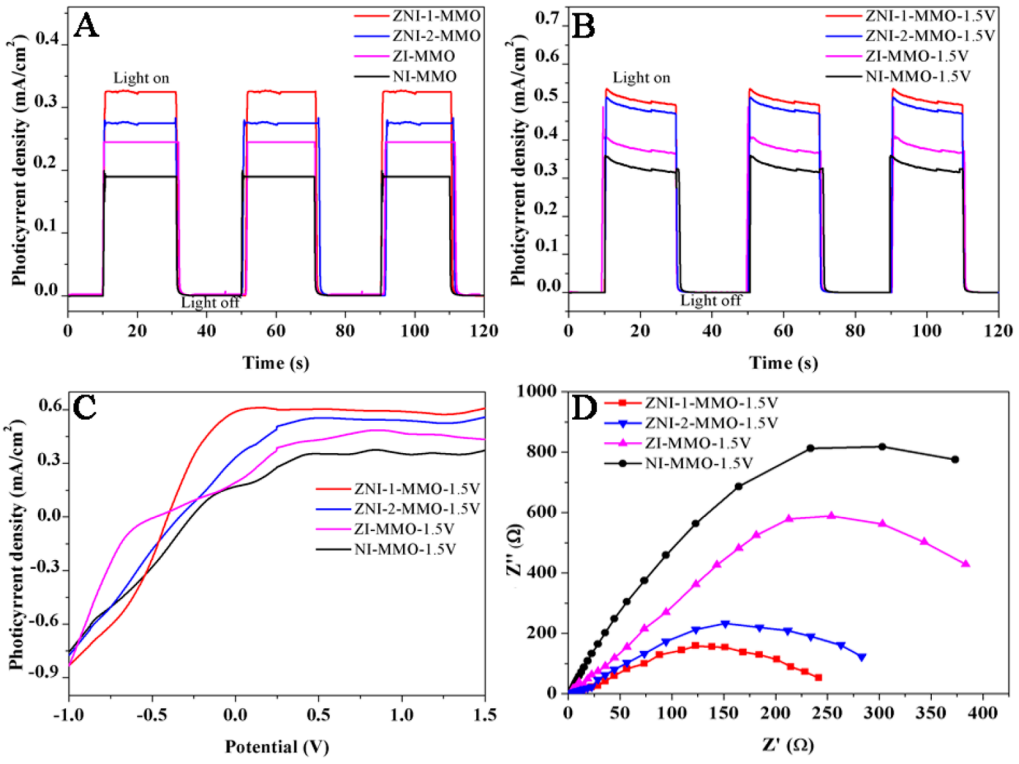


**Figure 13.** Photocurrent response of *I*−*t* (without bias potential (A) and with 1.5 V bias potential (B)) and *I*−*V* (C) curves, and EIS Nyquist plots (D) of the different samples.

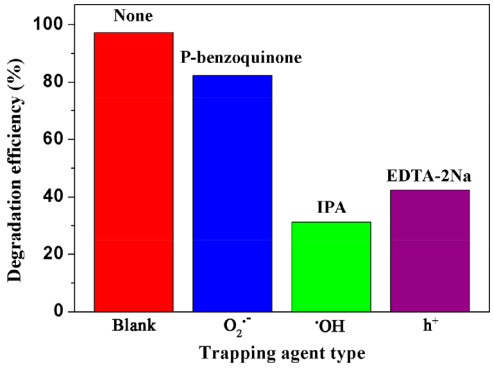


**Figure 14.** Effect of trapping agents (IPA, P-Benzoquinone and EDTA-2Na) on photoelectrodegradation of MB in an aqueous solution in the presence of ZNI-1-MMO-1.5 V.

Figure 15, and the detailed reaction process is represented in eqs 4−13.

$$In_2O_3 + \text{visible light} \rightarrow In_2O_3\,(e^-) + In_2O_3\,(h^+) \quad (4)$$

$$NiO + \text{visible light} \rightarrow NiO\,(e^-) + NiO\,(h^+) \quad (5)$$

$$ZnO + \text{visible light} \rightarrow ZnO\,(e^-) + ZnO\,(h^+) \quad (6)$$

$$p\text{-}NiO/n\text{-}In_2O_3 + \text{visible light} \rightarrow p\text{−}n\ NiO/In_2O_3\,(e^- + h^+) \quad (7)$$

$$p\text{-}NiO/n\text{-}ZnO + \text{visible light} \rightarrow p\text{−}n\ Nio/ZnO\,(e^- + h^+) \quad (8)$$

$$e^- + O_2 \rightarrow O_2^{\bullet -} \quad (9)$$

$$h^+ + H_2O \rightarrow {}^{\bullet}OH + H^+ \quad (10)$$

$$MB + O_2^{\bullet -} \rightarrow CO_2 + H_2O + \text{Other products} \quad (11)$$

$$MB + h^+ \rightarrow CO_2 + H_2O + \text{Other products} \quad (12)$$

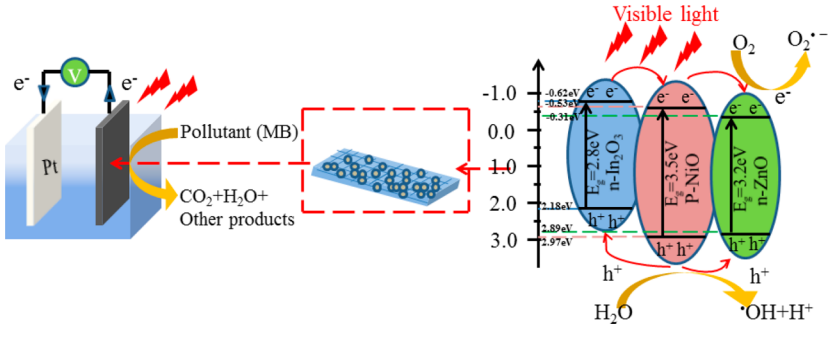


**Figure 15.** Schematic illustration of the photoelectrocatalytic mechanism of organic pollutant MB over the ZNI-1-MMO-1.5 V photoelectrode.



DOI: 10.1021/acs.iecr.8b04829
Ind. Eng. Chem. Res. 2019, 58, 836−848

$$MB + {}^{\bullet}OH \rightarrow CO_2 + H_2O + \text{Other products} \quad (13)$$

The overall photoelectrocatalytic degradation process include three successive steps: absorption and capture of visible light, separation and transfer of electrons and holes under visible light stimulation, and the surface redox reaction between active radicals and the target pollutants.[14] Under visible light irradiation, the photogenerated $h^+$ and $e^-$ are in their valence band (VB) and conduction band (CB), respectively (eqs 4–6).[69] In the ternary ZNI-1-MMO system, since the CB of $In_2O_3$ is higher than that of NiO and ZnO, the photoexcited electrons in the CB of $In_2O_3$ can be transferred to NiO and ZnO in turn. At the same time, since the VB of NiO is lower than that of $In_2O_3$ and ZnO, the holes generated by photoexcitation in the NiO VB can be transferred to $In_2O_3$ and ZnO. More importantly, when p-NiO is loaded with n-$In_2O_3$ or n-ZnO nanoparticles, a p–n heterojunction between the two semiconductors is formed. The heterostructures of p–n NiO/$In_2O_3$ or p–n NiO/ZnO could speed up the delivery of electrons in the interface (eqs 7 and 8).[70,71] Meanwhile, a suitable bias voltage can help the photogenerated electrons move rapidly to external circuit, which greatly reduces the recombination of photogenerated electrons and holes.[72] Electrons ($e^-$) and holes ($h^+$) can convert $O_2$ and $H_2O$ into $O_2^{\bullet-}$ and $^{\bullet}OH$ respectively (eqs 9 and 10). These active species ($^{\bullet}OH$, $h^+$, and $O_2^{\bullet-}$) have strong oxidation abilities and can degrade the organic pollutant MB efficiently (eqs 11–13).[64]

## 4. CONCLUSIONS

In summary, effective degradation of organic pollutant MB was achieved through the photoelectric catalysis using the ternary ZNI-1-MMO photoelectrodes. A MB degradation efficiency of 97.2% was achieved in 3 h with visible light irradiation and a bias potential of 1.5 V using ZNI-1-MMO, which exceeded the performance of ZNI-MMO photoelectrodes with other Ni/In molar ratios as well as single photocatalysis and electrolysis. In this PEC system, both $^{\bullet}OH$ and $h^+$ play a dominant role in the degradation of organic pollutant MB. The excellent photoelectrocatalytic activity could be attributed to the narrow band gap energy, strong visible light absorption capacity, high charge separation efficiency, and the double p–n heterojunction structure (p–n NiO/$In_2O_3$ and p–n NiO/ZnO) of the sample. Moreover, the ZNI-1-MMO-1.5 V photoelectrode can also be conveniently reused with a stable performance in MB degradation. Therefore, this work can provide a new strategy to improve the degradation of organic pollutants and promote the application of photoelectrochemical systems with photocatalysts rather than metals, polymers, ceramics, or their nanocomposites[73−83] for the purification of industrial wastewater.

## AUTHOR INFORMATION


### Corresponding Authors

*E-mail: shengsge@gmail.com (S.G.).
*E-mail: maixianmin@foxmail.com (X.M.).
*E-mail: dingtao@henu.edu.cn (T.D.).
*E-mail: a.subramania@gmail.com (S.A.).
*E-mail: zguo10@utk.edu (Z.G.).

### ORCID

Hu Liu: 0000-0003-3840-8135
Zhanhu Guo: 0000-0003-0134-0210


### Notes

The authors declare no competing financial interest.

## ACKNOWLEDGMENTS

This project was partially supported by the research gift fund from Engineered Multifunctional Composites (EMC) Nanotechnology LLC, Knoxville, TN USA and by National Natural Science Foundation of China (51508484).

## REFERENCES


(1) Yang, X.; You, F.; Zhao, Y.; Bai, Y.; Shao, L. Confinedly assembling surface nanocoating to manipulate nanofiltration membranes for highly-efficient dye removal. *ES Energy. Environ* **2018**, *1*, 106–113.
(2) Wang, Z.; Zhu, H.; Cao, N.; Du, R.; Liu, Y.; Zhao, G. Superhydrophobic surfaces with excellent abrasion resistance based on benzoxazine/mesoporous $SiO_2$. *Mater. Lett.* **2017**, *186*, 274–278.
(3) Jonstrup, M.; Kumar, N.; Murto, M.; Mattiasson, B. Sequential anaerobic–aerobic treatment of azo dyes: Decolourisation and amine degradability. *Desalination* **2011**, *280*, 339–346.
(4) Jonidi Jafari, A.; Kakavandi, B.; Jaafarzadeh, N.; Rezaei Kalantary, R.; Ahmadi, M.; Akbar Babaei, A. Fenton-like catalytic oxidation of tetracycline by AC@$Fe_3O_4$ as a heterogeneous persulfate activator: Adsorption and degradation studies. *J. Ind. Eng. Chem.* **2017**, *45*, 323–333.
(5) Su, T.; Shao, Q.; Qin, Z.; Guo, Z.; Wu, Z. Role of interfaces in two-dimensional photocatalyst for water splitting. *ACS Catal.* **2018**, *8*, 2253–2276.
(6) Park, H.; Bak, A.; Ahn, Y. Y.; Choi, J.; Hoffmannn, M. R. Photoelectrochemical performance of multi-layered $BiO_x$–$TiO_2$/Ti electrodes for degradation of phenol and production of molecular hydrogen in water. *J. Hazard. Mater.* **2012**, *211-212*, 47–54.
(7) Huang, H.; Xiao, K.; He, Y.; Zhang, T.; Dong, F.; Du, X.; Zhang, Y. *In situ* assembly of BiOI@$Bi_{12}O_{17}Cl_2$*p-n* junction: charge induced unique front-lateral surfaces coupling heterostructure with high exposure of BiOI {001} active facets for robust and nonselective photocatalysis. *Appl. Catal., B* **2016**, *199*, 75–86.
(8) Giordano, F.; Abate, A.; Correa Baena, J. P.; Saliba, M.; Matsui, T.; Im, S. H.; Zakeeruddin, S. M.; Nazeeruddin, M. K.; Hagfeldt, A.; Graetzel, M. Enhanced electronic properties in mesoporous $TiO_2$ via lithium doping for high-efficiency perovskite solar cells. *Nat. Commun.* **2016**, *7*, 10379.
(9) Lee, K. M.; Lai, C. W.; Ngai, K. S.; Juan, J. C. Recent developments of zinc oxide based photocatalyst in water treatment technology: A review. *Water Res.* **2016**, *88*, 428–448.
(10) Shindume L, H.; Zhao, Z.; Wang, N.; Liu, H.; Umar, A.; Zhang, J.; Wu, T.; Guo, Z. Enhanced photocatalytic activity of B, N-codoped $TiO_2$ by a new molten nitrate process. *J. Nanosci. Nanotechnol.* **2019**, *19*, 839–949.
(11) Liu, D.; Liu, T.; Zhang, L.; Qu, F.; Du, G.; Asiri, A. M.; Sun, X. High-performance urea electrolysis towards less energy-intensive electrochemical hydrogen production using a bifunctional catalyst electrode. *J. Mater. Chem. A* **2017**, *5*, 3208–3213.
(12) Zhang, L.; Qin, M.; Yu, W.; Zhang, Q.; Xie, H.; Sun, Z.; Shao, Q.; Guo, X.; Hao, L.; Zheng, Y.; Guo, Z. Heterostructured $TiO_2$/$WO_3$ nanocomposites for photocatalytic degradation of toluene under visible light. *J. Electrochem. Soc.* **2017**, *164*, H1086–H1090.
(13) Tian, J.; Shao, Q.; Dong, X.; Zheng, J.; Pan, D.; Zhang, X.; Cao, H.; Hao, L.; Liu, J.; Mai, X.; et al. Bio-template synthesized NiO/C hollow microspheres with enhanced Li-ion battery electrochemical performance. *Electrochim. Acta* **2018**, *261*, 236–245.
(14) Zhang, Y.; Qian, L.; Zhao, W.; Li, X.; Huang, X.; Mai, X.; Wang, Z.; Shao, Q.; Yan, X.; Guo, Z. Highly efficient Fe-N-C nanoparticles modified porous graphene composites for oxygen reduction reaction. *J. Electrochem. Soc.* **2018**, *165*, H510–H516.
(15) Ma, Y.; Ma, M.; Yin, X.; Shao, Q.; Lu, N.; Feng, Y.; Lu, Y.; Wujcik, E. K.; Mai, X.; Wang, C.; Guo, Z. Tuning polyaniline nanostructures via end group substitutions and their morphology



DOI: 10.1021/acs.iecr.8b04829
*Ind. Eng. Chem. Res.* 2019, 58, 836–848

dependent electrochemical performances. *Polymer* **2018**, *156*, 128−135.
(16) Seol, M.; Jang, J. W.; Cho, S.; Lee, J. S.; Yong, K. Highly efficient and stable cadmium chalcogenide quantum dot/ZnO nanowires for photoelectrochemical hydrogen generation. *Chem. Mater.* **2013**, *25*, 184−189.
(17) Tang, J.; Zhang, Y.; Kong, B.; Wang, Y.; Da, P.; Li, J.; Elzatahry, A. A.; Zhao, D.; Gong, X.; Zheng, G. Solar-driven photoelectrochemical probing of nanodot/nanowire/cell interface. *Nano Lett.* **2014**, *14*, 2702−2708.
(18) Fernández-Domene, R. M.; Sánchez-Tovar, R.; Lucas-Granados, B.; García-Zamora, C. S.; García-Antón, J. Customized $WO_3$ nanoplatelets as visible-light photoelectrocatalyst for the degradation of a recalcitrant model organic compound (methyl orange). *J. Photochem. Photobiol., A* **2018**, *356*, 46−56.
(19) Sun, Y.; Liu, C.; Grauer, D. C.; Yano, J.; Long, J. R.; Yang, P.; Chang, C. J. Electrodeposited cobalt-sulfide catalyst for electrochemical and photoelectrochemical hydrogen generation from water. *J. Am. Chem. Soc.* **2013**, *135*, 17699−17702.
(20) Kirner, J. T.; Stracke, J. J.; Gregg, B. A.; Finke, R. G. Visible-Light-Assisted Photoelectrochemical Water Oxidation by Thin Films of a Phosphonate-Functionalized Perylene Diimide Plus $CoO_x$Cocatalyst. *ACS Appl. Mater. Interfaces* **2014**, *6*, 13367−13377.
(21) Yang, L.; Wang, X.; Mai, X.; Wang, T.; Wang, C.; Li, X.; Murugadoss, V.; Shao, Q.; Angaiah, S.; Guo, Z. Constructing efficient mixed-ion perovskite solar cells based on $TiO_2$ nanorod array. *J. Colloid Interface Sci.* **2019**, *534*, 459−468.
(22) Fujishima, A.; Rao, T. N.; Tryk, D. A. Titanium dioxide photocatalysis. *J. Photochem. Photobiol., C* **2000**, *1*, 1−21.
(23) Zhang, J. Y.; Xue, X. Z.; Liu, J. K. Eminently Enhanced Anticorrosion Performance and Mechanisms of X-ZnO (X= C, N, and P) Solid Solutions. *Inorg. Chem.* **2017**, *56*, 12260−12271.
(24) Deng, X.; Zhang, H.; Ma, Q.; Cui, Y.; Cheng, X.; Li, X.; Xie, M.; Cheng, Q. Fabrication of p-NiO/n-$TiO_2$ nano-tube arrays photoelectrode and its enhanced photocatalytic performance for degradation of 4-chlorphenol. *Sep. Purif. Technol.* **2017**, *186*, 1−9.
(25) Zhang, X.; Yu, S.; Cao, Y.; Chen, L.; Zhao, T.; Yang, F. $Cu_2O$-coated polystyrene microsphere materials with enhanced photo- and photoelectro-catalytic activity. *J. Solid State Electrochem.* **2013**, *17*, 1429−1434.
(26) Zhu, Q.; Zhang, Y.; Wang, J.; Zhou, F.; Chu, P. K. Microwave Synthesis of Cuprous Oxide Micro-/Nanocrystals with Different Morphologies and Photocatalytic Activities. *J. Mater. Sci. Technol.* **2011**, *27*, 289−295.
(27) Zhao, J.; Ge, S.; Pan, D.; Shao, Q.; Lin, J.; Wang, Z.; Hu, Z.; Wu, T.; Guo, Z. Solvothermal synthesis, characterization and photocatalytic property of zirconium dioxide doped titanium dioxide spinous hollow microspheres with sunflower pollen as bio-templates. *J. Colloid Interface Sci.* **2018**, *529*, 111−121.
(28) Shi, J. Preparation of Fe (III) and Ho (III) co-doped $TiO_2$ films loaded on activated carbon fibers and their photocatalytic activities. *Chem. Eng. J.* **2009**, *151*, 241−246.
(29) Evans, D. G.; Slade, R. C. T. Structural aspects of layered double hydroxides. *Struct. Bonding (Berlin)* **2005**, *119*, 1−87.
(30) Ezeh, Ci.; Tomatis, M.; Yang, X.; He, J.; Sun, C. Ultrasonic and hydrothermal mediated synthesis routes for functionalized Mg-Al LDH: Comparison study on surface morphology, basic site strength, cyclic sorption. *Ultrason. Sonochem.* **2018**, *40*, 341−352.
(31) Li, R.; Che, R.; Liu, Q.; Su, S.; Li, Z.; Zhang, H.; Liu, J.; Liu, L.; Wang, J. Hierarchically structured layered-double-hydroxides derived by ZIF-67 for uranium recovery from simulated seawater. *J. Hazard. Mater.* **2017**, *338*, 167−176.
(32) Meng, W.; Li, F.; Evans, D. G.; Duan, X. Preparation and thermal decomposition of magnesium/iron (III) layered double hydroxide intercalated by hexacyanoferrate (III) ions. *J. Mater. Sci.* **2004**, *39*, 4655−4657.
(33) Huang, L.; Chu, S.; Wang, J. Q.; Kong, F.; Luo, L. L.; Wang, Y.; Zou, Z. G. Novel visible light driven Mg−Zn−In ternary layered materials for photocatalytic degradation of methylene blue. *Catal. Today* **2013**, *212*, 81−88.
(34) Becker, C. M.; Gabbardo, A. D.; Wypych, F.; Amico, S. C. Mechanical and flame-retardant properties of epoxy/Mg−Al LDH composites. *Composites, Part A* **2011**, *42*, 196−202.
(35) Mendoza-Damián, G.; Tzompantzi, F.; Mantilla, A.; Barrera, A.; Lartundo-Rojas, L. Photocatalytic degradation of 2, 4-dichlorophenol with MgAlTi mixed oxides catalysts obtained from layered double hydroxides. *J. Hazard. Mater.* **2013**, *263*, 67−72.
(36) Chen, G.; Qian, S.; Tu, X.; Wei, X.; Zou, J.; Leng, L.; Luo, S. Enhancement photocatalytic degradation of rhodamine B on nanoPt intercalated Zn−Ti layered double hydroxides. *Appl. Surf. Sci.* **2014**, *293*, 345−351.
(37) Zhang, L.; Dai, C.; Zhang, X.; Liu, Y.; Yan, J. Synthesis and highly efficient photocatalytic activity of mixed oxides derived from ZnNiAl layered double hydroxides. *Trans. Nonferrous Met. Soc. China* **2016**, *26*, 2380−2389.
(38) Huang, D.; Ma, J.; Fan, C.; Wang, K.; Zhao, W.; Peng, M.; Komarneni, S. Co-Mn-Fe complex oxide catalysts from layered double hydroxides for decomposition of methylene blue: Role of Mn. *Appl. Clay Sci.* **2018**, *152*, 230−238.
(39) Wang, K.; Ma, J.; Yao, Z.; Zhang, W.; Komarneni, S. Synthesis and photocatalytic properties of new ternary Ni−Fe−Cr hydrotalcite-like compounds. *Ceram. Int.* **2016**, *42*, 15981−15988.
(40) Pan, D.; Ge, S.; Zhao, J.; Shao, Q.; Guo, L.; Zhang, X.; Lin, J.; Xu, G.; Guo, Z. Synthesis, Characterization and Photocatalytic Activity of Mixed-metal Oxides Derived from NiCoFe Ternary Layered Double Hydroxides. *Dalton Trans* **2018**, *47*, 9765−9778.
(41) Carvalho, D. C.; Ferreira, N. A.; Filho, J. M.; Ferreira, O. P.; Soares, J. M.; Oliveira, A. C. Ni−Fe and Co−Fe binary oxides derived from layered double hydroxides and their catalytic evaluation for hydrogen production. *Catal. Today* **2015**, *250*, 155−165.
(42) Li, Y. N.; Su, J.; Lv, X. Y.; Long, Y. F.; Wen, Y. X. Yeast biotemplate synthesis of porous anatase $TiO_2$ and potential application as an anode for sodium-ion batteries. *Electrochim. Acta* **2015**, *182*, 596−603.
(43) Mendoza-Damián, G.; Tzompantzi, F.; Mantilla, A.; Barrera, A.; Lartundo-Rojas, L. Photocatalytic degradation of 2, 4-dichlorophenol with MgAlTi mixed oxides catalysts obtained from layered double hydroxides. *J. Hazard. Mater.* **2013**, *263*, 67−72.
(44) Xiang, X.; Xie, L.; Li, Z.; Li, F. Ternary MgO/ZnO/$In_2O_3$ heterostructured photocatalysts derived from a layered precursor and visible-light-induced photocatalytic activity. *Chem. Eng. J.* **2013**, *221*, 222−229.
(45) Zhang, L.; Dai, C.; Zhang, X.; Liu, Y.; Yan, J. Synthesis and highly efficient photocatalytic activity of mixed oxides derived from ZnNiAl layered double hydroxides. *Trans. Nonferrous Met. Soc. China* **2016**, *26*, 2380−2389.
(46) Guo, Y.; Gong, Z.; Li, P.; Zhang, W.; Gao, B. Preparation, characterization and enhancement of the visible-light photocatalytic activity of $In_2O_3$/Na-bentonite composite. *Ceram. Int.* **2016**, *42*, 8850−8855.
(47) Sánchez-Cantú, M.; Hernández-Torres, M. E.; Castillo-Navarro, A.; Cadena-Torres, E.; Rubio-Rosas, E.; Gracia-Jiménez, J. M.; Tzompantzi, F. Evaluation of hydrotalcite-like compounds with distinct interlaminar anions as catalyst precursors in methylene blue photodegradation. *Appl. Clay Sci.* **2017**, *135*, 1−8.
(48) Ahmed, A. A. A.; Talib, Z. A.; Hussein, M. Z. Influence of sodium dodecyl sulfate concentration on the photocatalytic activity and dielectric properties of intercalated sodium dodecyl sulfate into Zn−Cd−Al layered double hydroxide. *Mater. Res. Bull.* **2015**, *62*, 122−131.
(49) Sahu, R. K.; Mohanta, B. S.; Das, N. N. Synthesis, characterization and photocatalytic activity of mixed oxides derived from ZnAlTi ternary layered double hydroxides. *J. Phys. Chem. Solids* **2013**, *74*, 1263−1270.
(50) Zhang, P.; Shi, H.; Xiuxiu, R.; Guangren, Q.; Frost, R. L. Na-dodecylsulfate modification of hydrocalumite and subsequent effect


DOI: 10.1021/acs.iecr.8b04829
*Ind. Eng. Chem. Res.* 2019, 58, 836−848

on the structure and thermal decomposition. *J. Therm. Anal. Calorim.* **2011**, *104*, 743−747.
(51) Shao, M.; Han, J.; Wei, M.; Evans, D. G.; Duan, X. The synthesis of hierarchical Zn−Ti layered double hydroxide for efficient visible-light photocatalysis. *Chem. Eng. J.* **2011**, *168*, 519−524.
(52) Li, Y. N.; Su, J.; Lv, X. Y.; Long, Y. F.; Wen, Y. X. Yeast biotemplate synthesis of porous anatase $TiO_2$ and potential application as an anode for sodium-ion batteries. *Electrochim. Acta* **2015**, *182*, 596−603.
(53) Shakeel, M.; Li, B.; Yasin, G.; Arif, M.; Rehman, W.; Khan, H. D. In situ fabrication of foamed titania carbon nitride nanocomposite and its synergetic visible light photocatalytic performance. *Ind. Eng. Chem. Res.* **2018**, *57*, 8152−8159.
(54) Pan, D.; Ge, S.; Zhang, X.; Mai, X.; Li, S.; Guo, Z. Synthesis and photoelectrocatalytic activity of $In_2O_3$ hollow microspheres via a bio-template route using yeast templates. *Dalton Trans* **2018**, *47*, 708−715.
(55) Qwabe, L. Q.; Friedrich, H. B.; Singh, S. Preferential oxidation of CO in a hydrogen rich feed stream using Co−Fe mixed metal oxide catalysts prepared from hydrotalcite precursors. *J. Mol. Catal. A: Chem.* **2015**, *404*, 167−177.
(56) Li, M.; Li, X.; Jiang, G.; He, G. Hierarchically macro−mesoporous $ZrO_2$−$TiO_2$ composites with enhanced photocatalytic activity. *Ceram. Int.* **2015**, *41*, 5749−5757.
(57) Sun, X.; Liu, X.; Deng, X.; Xu, X. Synthesis of Zn-doped $In_2O_3$ nano sphere architectures as a triethylamine gas sensor and photocatalytic properties. *RSC Adv.* **2016**, *6*, 89847−89854.
(58) Li, X.; Wang, L.; Zhang, L.; Zhuo, S. A facile route to the synthesis of magnetically separable BiOBr/$NiFe_2O_4$ composites with enhanced photocatalytic performance. *Appl. Surf. Sci.* **2017**, *419*, 586−594.
(59) Tang, J. W.; Zou, Z. G.; Ye, J. H. Photophysical and Photocatalytic Properties of $AgInW_2O_8$. *J. Phys. Chem. B* **2003**, *107*, 14265−14269.
(60) Zhang, L.; Yu, W.; Han, C.; Guo, J.; Zhang, Q.; Xie, H.; Shao, Q.; Sun, Z.; Guo, Z. Large scaled synthesis of heterostructured electrospun $TiO_2$/$SnO_2$ nanofibers with an enhanced photocatalytic activity. *J. Electrochem. Soc.* **2017**, *164*, H651−H656.
(61) Zhao, X.; Wang, L.; Xu, X.; Lei, X.; Xu, S.; Zhang, F. Fabrication and photocatalytic properties of novel ZnO/$ZnAl_2O_4$ nanocomposite with $ZnAl_2O_4$ dispersed inside ZnO network. *AIChE J.* **2012**, *58*, 573−582.
(62) Sun, M.; Chen, G.; Zhang, Y.; Wei, Q.; Ma, Z.; Du, B. Efficient Degradation of Azo Dyes over $Sb_2S_3$/$TiO_2$ Heterojunction under Visible Light Irradiation. *Ind. Eng. Chem. Res.* **2012**, *51*, 2897−2903.
(63) Li, J.; Li, L.; Zheng, L.; Xian, Y.; Jin, L. Photoelectrocatalytic degradation of rhodamine B using Ti/$TiO_2$ electrode prepared by laser calcination method. *Electrochim. Acta* **2006**, *51*, 4942−4949.
(64) Zhao, B.; Shao, Q.; Hao, L.; Zhang, L.; Liu, Z.; Zhang, B.; Ge, S.; Guo, Z. Yeast-template synthesized Fe-doped cerium oxide hollow microspheres for visible photodegradation of acid orange 7. *J. Colloid Interface Sci.* **2018**, *511*, 39−47.
(65) Guo, T.; Dang, C.; Tian, S.; Wang, Y.; Cao, D.; Gong, Y.; Zhao, S.; Mao, R.; Yang, B.; Zhao, X. Persulfate enhanced photoelectrocatalytic degradation of cyanide using a $CuFe_2O_4$ modified graphite felt cathode. *Chem. Eng. J.* **2018**, *347*, 535−542.
(66) Chen, W.; Wu, W.; Yang, W.; Zhao, J.; Xiao, M.; Kong, W. $CdCl_2$-assisting heat-treatment: enhanced photoelectrocatalytic hydrogen generation and stability of CdS/ZnO nanoheterojunction arrays. *Int. J. Hydrogen Energy* **2018**, *43*, 9969−9977.
(67) Kirubasankar, B.; Murugadoss, V.; Lin, J.; Ding, T.; Dong, M.; Liu, H.; Zhang, J.; Li, T.; Wang, N.; Guo, Z.; et al. In-situ grown nickel selenide onto graphene nanohybrid electrodes for high energy density asymmetric supercapacitors. *Nanoscale* **2018**, *10*, 20414−20425.
(68) Song, B.; Wang, T.; Sun, H.; Shao, Q.; Zhao, J.; Song, K.; Hao, L.; Wang, L.; Guo, Z. Two-step hydrothermally synthesized carbon nanodots/$WO_3$ photocatalysts with enhanced photocatalytic performance. *Dalton Trans* **2017**, *46*, 15769−15777.
(69) Tachikawa, T.; Fujitsuka, A. M.; Majima, T. Mechanistic insight into the $TiO_2$ photocatalytic reactions: design of new photocatalysts. *J. Phys. Chem. C* **2007**, *111*, 5259−5275.
(70) Yan, J.; Yang, S.; Xie, Z.; Li, X.; Zhou, W.; Zhang, X.; Fang, Y.; Zhang, S.; Peng, F. Heterostructured CoO/3D-$TiO_2$ nanorod arrays for photoelectrochemical water splitting hydrogen production. *J. Solid State Electrochem.* **2017**, *21*, 455−461.
(71) Li, S.; Hu, S.; Xu, K.; Jiang, W.; Liu, Y.; Leng, Z.; Liu, J. Construction of fiber-shaped silver oxide/tantalum nitride pn heterojunctions as highly efficient visible-light-driven photocatalysts. *J. Colloid Interface Sci.* **2017**, *504*, 561−569.
(72) Chen, D.; Yang, J.; Zhu, Y.; Zhang, Y.; Zhu, Y. Fabrication of BiOI/graphene hydrogel/FTO photoelectrode with 3D porous architecture for the enhanced photoelectrocatalytic performance. *Appl. Catal., B* **2018**, *233*, 202−212.
(73) Wang, C.; Mo, B.; He, Z.; Zhao, C. X.; Xie, X.; Zhang, L.; Shao, Q.; Guo, X.; Wujcik, E.; Guo, Z. Hydroxide ions transportation in polynorbornene anion exchange membrane. *Polymer* **2018**, *138*, 363−368.
(74) Zhao, Z.; Guan, R.; Zhang, J.; Zhao, Z.; Bai, P. Effects of process parameters of semisolid stirring on microstructure of Mg-3Sn-1Mn-3SiC (wt%) strip processed by rheo-rolling. *Acta Metall. Sin. (Engl. Lett.)* **2017**, *30*, 66−72.
(75) Zhao, Z.; Bai, P.; Guan, R.; Murugadoss, V.; Liu, H.; Wang, X.; Guo, Z. Microstructural evolution and mechanical strengthening mechanism of Mg-3Sn-1Mn-1La alloy after heat treatments. *Mater. Sci. Eng., A* **2018**, *734*, 200−209.
(76) Du, W.; Wang, X.; Zhan, J.; Sun, X.; Kang, L.; Jiang, F.; Zhang, X.; Shao, Q.; Dong, M.; Liu, H.; Murugadoss, V.; Guo, Z. Biological cell template synthesis of nitrogen-doped porous hollow carbon spheres/$MnO_2$ composites for high-performance asymmetric supercapacitors. *Electrochim. Acta* **2019**, *296*, 907−915.
(77) Wang, C.; Mo, B.; He, Z.; Shao, Q.; Pan, D.; Wujick, E.; Guo, J.; Xie, X.; Xie, X.; Guo, Z. Crosslinked norbornene copolymer anion exchange membrane for fuel cells. *J. Membr. Sci.* **2018**, *556*, 118−125.
(78) Wang, C.; He, Z.; Xie, X.; Mai, X.; Li, Y.; Li, T.; Zhao, M.; Yan, C.; Liu, H.; Wujcik, E.; Guo, Z. Controllable cross-linking anion exchange membranes with excellent mechanical and thermal properties. *Macromol. Mater. Eng.* **2018**, *303*, 1700462.
(79) Du, H.; Zhao, C.; Lin, J.; Hu, Z.; Shao, Q.; Guo, J.; Wang, B.; Pan, D.; Wujcik, E. K.; Guo, Z. Carbon nanomaterials in direct liquid fuel cells. *Chem. Rec.* **2018**, *18*, 1365−1372.
(80) Zhao, Z.; An, H.; Lin, J.; Feng, M.; Murugadoss, V.; Ding, T.; Liu, H.; Shao, Q.; Mai, X.; Wang, N. et al. Progress on the photocatalytic reduction removal of chromium contamination. *Chem. Rec.*, **2018**, DOI: 10.1002/tcr.201800153.
(81) Zhao, Z.; Misra, R.; Bai, P.; Gao, J.; Li, Y.; Guan, R.; Guo, Z.; Liu, H. Novel process of coating Al on graphene involving organic aluminum accompanying microstructure evolution. *Mater. Lett.* **2018**, *232*, 202−205.
(82) Wang, Z.; Zhu, H.; Cao, N.; Du, R.; Liu, Y.; Zhao, G. Superhydrophobic surfaces with excellent abrasion resistance based on benzoxazine/mesoporous $SiO_2$. *Mater. Lett.* **2017**, *186*, 274−278.
(83) Zhao, Y.; Qi, L.; Jin, Y.; Wang, K.; Tian, J.; Han, P. The structural, elastic, electronic properties and Debye temperature of $D0_{22}$-$Ni_3V$ under pressure from first-principles. *J. Alloys Compd.* **2015**, *647*, 1104−1110.


DOI: 10.1021/acs.iecr.8b04829
*Ind. Eng. Chem. Res.* 2019, 58, 836−848